Solar Water Splitting by TiO_2/CdS/Co–Pi Nanowire Array Photoanode Enhanced with Co–Pi as Hole Transfer Relay and CdS as Light Absorber

Guanjie Ai, Hongxing Li, Shaopei Liu, Rong Mo, and Jianxin Zhong**

The cobalt phosphate water oxidation catalyst (Co–Pi WOC) stabilized, CdS sensitized TiO_2 nanowire arrays for nonsacrificial solar water splitting are reported. In this TiO_2/CdS/Co–Pi photoanode, the Co–Pi WOC acts as hole transfer relay to accelerate the surface water oxidation reaction, CdS serves as light absorber for wider solar spectra harvesting, and TiO_2 matrix provides direct pathway for electron transport. This triple TiO_2/CdS/Co–Pi hybrid photoanode exhibits much enhanced photocurrent density and negatively shifts in onset potential, resulting in 1.5 and 3.4 times improved photoconversion efficiency compared to the TiO_2/CdS and TiO_2 photoanode, respectively. More importantly, the TiO_2/CdS/Co–Pi shows significantly improved photoelectrochemical stability compared to the TiO_2/CdS electrode, with ≈72% of the initial photocurrent retained after 2 h irradiation. The reason for the promoted performance is discussed in detail based on electrochemical measurements. This work provides a new paradigm for designing 1D nanoframework/light absorber/WOC photoanode to simultaneously enhance light absorption, charge separation, and transport and surface water oxidation reaction for efficient and stable solar fuel production.

1. Introduction

To exploit the potential benefits of sunlight as renewable and carbon-neutral power source, it is necessary to develop a practical technique for the solar energy conversion and storing. In nature, the sunlight is harvested and stored in the form of chemical fuel by photosynthesis.[1] Out of the leaves, the natural photosynthesis processes is duplicated by the photoelectrochemical (PEC) cell, which converts sunlight into spatially separated hole–electron pairs and then uses them to oxidize and reduce water into O_2 and H_2 molecules.[2] The key component of a PEC cell is the semiconducting photoelectrode, of which the material and structure both play critical roles in this artificial photosynthesis system.[3,4] Varieties of photoelectrodes have been investigated and optimized to improve PEC performances based on these considerations: high stability in aqueous solution, small band gap for wide spectrum response, proper conduction/valence band position satisfying water oxidization and reduction potentials, effective carrier separation and transportation, fast surface chemical reactions (charge utilization), etc.[5] However, no single material can meet all of these requirements so far.

Fortunately, the hetero-structurization of semiconductors provides a feasible method for integrating the merits of different materials into one single photoelectrode, which usually presents promoted or new physicochemical properties.[6] One of the most classic examples of the heterostructured photoelectrode is the 1D metal-oxide semiconductor sensitized with II–VI chalcogenides for PEC hydrogen production, such as cadmium sulfide (CdS) shells or quantum dots sensitized titanium dioxide (TiO_2) nanowire array photoanode.[7–10] In the TiO_2/CdS nanowire arrays, the TiO_2 serves as a nice backbone with its advantageous micro-architecture, high chemical stability, and easy fabrication. Meanwhile, the CdS works as light absorber to significantly extend the solar utilization into visible light region. Additionally, the type-II heterojunction interfaces in the TiO_2/CdS can profoundly improve the separation efficiency of photogenerated electron–hole pairs. Similar to this TiO_2/CdS prototype, lots of related heterostructures have been fabricated as photoanode, such as TiO_2/CdSe,[11–13] ZnO/CdS,[14,15] ZnO/CdSe,[16,17] ZnO/ZnSe,[18,19] TiO_2/CdS_xTe_{1-x},[20] TiO_2/CdS_xSe_{1-x},[21–24] ZnO/$Zn_xCd_{1-x}Se$,[25–27] ZnO/$Zn_xCd_{1-x}Te$,[28] etc. Albeit high photocurrent densities have been obtained by these metal-oxide/chalcogenide heterojunctions, their poor PEC stability owing to the hole-induced self-oxidative decomposition of the chalcogenide even in the presence of sacrificial reagent remains to be a major problem for their practical application in PEC hydrogen generation systems.[29,30] More importantly, nonsacrificial overall water splitting is the eventual goal of the community.

Recently, modifying semiconductor photoanode with water oxidation catalyst (WOC) has been an important research direction for improving the PEC stability as well as reducing the electron–hole recombination rate.[31–37] The WOC can change the water oxidation reaction mechanism and reduce reaction

G. Ai, Prof. H. Li, S. Liu, R. Mo,
Prof. J. Zhong
Hunan Key Laboratory for Micro-Nano
Energy Materials and Devices
School of Physics and Optoelectronics
Xiangtan University
Hunan 411105, P. R. China
E-mail: hongxinglee@xtu.edu.cn; jxzhong@txu.edu.cn

DOI: 10.1002/adfm.201502461

energy barrier, resulting in boosted surface chemical reaction rate. Among various WOC, cobalt phosphate (Co–Pi) emerges to be a hot candidates to couple with photocatalyst as cocatalyst due to its high abundance on earth, self-healing features, and functionality under benign conditions.[38] Although the enhancement mechanism for the photoanode by Co–Pi modification is still under debate, a generally acceptable explanation is that the photo-induced hole oxidizes the Co ion to higher oxidation state, which further oxidizes water molecules, and then returns to its initial oxidation state.[39–41] Many semiconductor materials have been coupled with the Co–Pi catalyst to exploit its merit as a cocatalyst.[42–44] For example, Li et al. reported a high and stable photocurrent obtained by combining the highly active Ta_3N_5 nanorods with Co–Pi catalyst.[45] In the previous work of our group, we reported a Co–Pi modified TiO_2 nanowire arrays for solar water splitting and the mechanism insights, which has shown enhanced PEC performance especially in the low bias potential region in wide pH value electrolyte from 1 to 14.[46]

In this work, we report the first demonstration of Co–Pi WOC modified metal oxide/chalcogenide heterostructure for solar water splitting in neutral electrolyte without sacrificial reagent. The typical TiO_2/CdS core/shell nanowire arrays are used for simplification. In this TiO_2/CdS/Co–Pi photoanode, the Co–Pi WOC acts as a hole transfer relay at the electrode/electrolyte interface to accelerate photohole output from electrode to electrolyte for fast water oxidation reaction, the CdS serves as light absorber for wide solar spectra harvesting, and the vertically aligned TiO_2 nanowire array works as the electron conductor for direct charge transfer to fluorine-doped tin oxide (FTO) glass collector as well as light trapper. The TiO_2/CdS/Co–Pi ternary composite photoanode shows enhanced photocurrent especially in the low bias region compared to the TiO_2/CdS photoanode. More importantly, the PEC stability of the TiO_2/CdS photoanode is significantly improved after the Co–Pi modification, with ≈72% of the initial photocurrent remained after 2 h persistent irradiation in the *i–t* curves test. Electrochemical impedance spectra indicate that the improved PEC performance is attributed to the accelerated charge transfer between the photoanode/electrolyte interfaces. The valence band potential of TiO_2, CdS, and the oxidation potential Co–Pi WOC are found to be a stepwise alignment by electrochemical analysis, which is also beneficial for the charge separation and transportation. This work provides a new paradigm for designing wide-band-gap semiconductor backbone/light absorber/WOC composite systems to simultaneously enhance light absorption, charge separation/transport and surface water oxidation reactions for efficient and stable solar fuel production.

2. Results and Discussions

The TiO_2 nanowire arrays were grown on FTO glass substrate by hydrothermal method and characterized by the scanning electron microscope (SEM) and transmission electron microscopy (TEM) observation. In **Figure 1**a, the tetragonal shaped

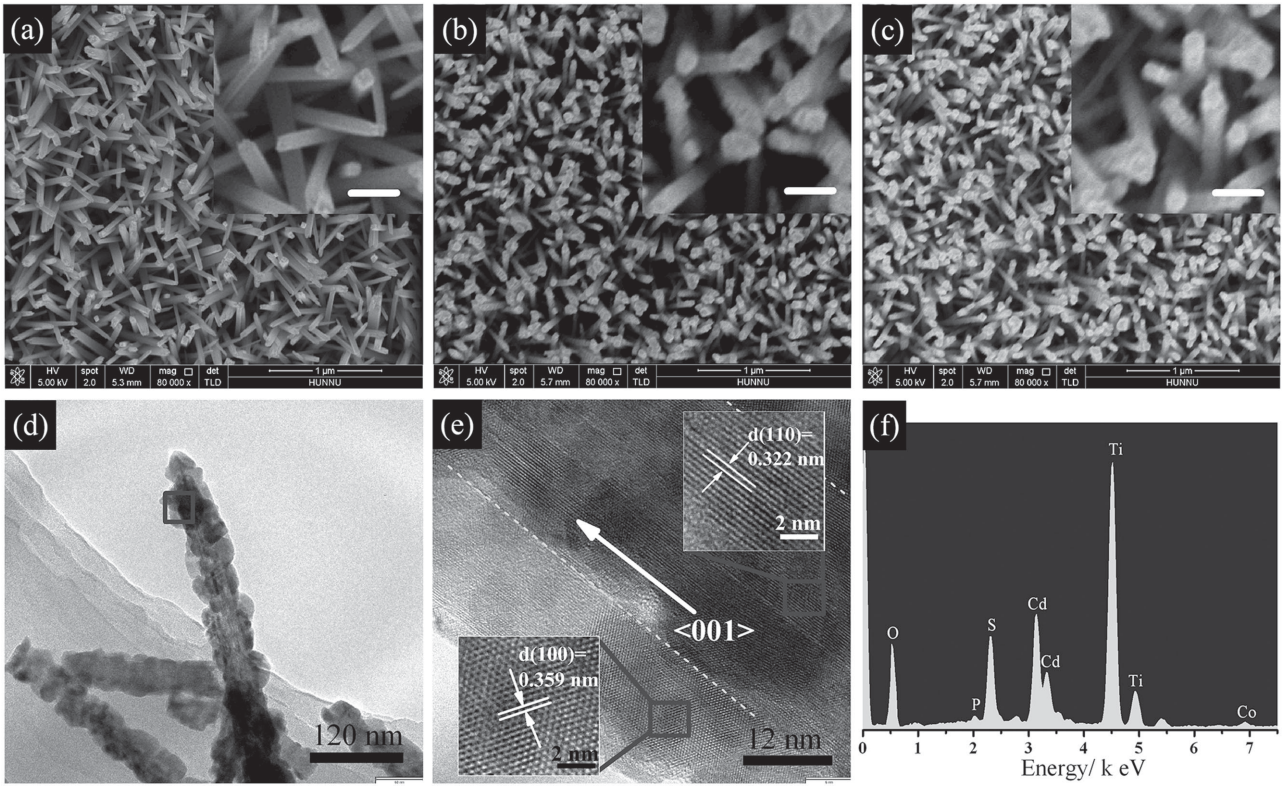

Figure 1. SEM images of a) pristine TiO_2, b) TiO_2/CdS, and c) TiO_2/CdS/Co–Pi nanowire arrays. The scale bars are all 150 nm in inserted enlarging SEM images. d) TEM and e) HRTEM images of the TiO_2/CdS/Co–Pi nanowire. f) EDS collected from the TiO_2/CdS/Co–Pi nanowire.

TiO_2 nanowires are quasi-vertically standing on the FTO substrate with diameter around 50 nm. After the coating of CdS layer by chemical vapor deposition method, the nanowires still keep their 1D geometry, but the surfaces become rough along the entire length with diameter increased to ≈80 nm (Figure 1b). In the SEM image of TiO_2/CdS/Co–Pi sample (Figure 1c), the photoelectrochemically deposited Co–Pi cannot be observed by the SEM observation, only representing somewhat brighter image than the TiO_2/CdS sample under the same measurement situation. This brighter image may be due to the changed surface condition (such as the electroconductivity or surface atomic species). Figure 1d shows the typical TEM image of the TiO_2/CdS/Co–Pi nanowires, from which it is observed that the tetragonal TiO_2 nanowire is completely encapsulated by CdS sheath, and the thickness of the shell is about 18 nm. In Figure 1e, the high resolution TEM image clearly reveals the interface of two distinct lattice fringes of 0.322 and 0.359 nm, corresponding to (110) and (100) lattice planes of the rutile TiO_2 and wurtzite CdS, respectively. The unobserved Co–Pi particles or clusters by SEM and TEM characterization in the TiO_2/CdS/Co–Pi sample may be ascribed to the molecular scale and/or amorphous property of Co–Pi. However, the existence of Co–Pi can be identified by the energy-dispersive X-ray spectroscopy (EDS) measurement as exhibited in Figure 1f as well as X-ray photoelectron spectroscopy (XPS) below.

XPS was used to examine the composition and chemical valence status of the TiO_2/CdS/Co–Pi sample. The full scan spectrum corroborates the existence of the Ti, O, Cd, S, P, and Co in the sample with no obvious impurities detected (**Figure 2**a). The measured atomic concentrations using XPS are determined to be 1.1% for Ti, 49.62% for O, 22.72% for Cd, 14.26% for S, 3.85% for Co, and 8.44% for P, respectively. The extremely low atomic ratio of the Ti is due to the limited probing depth of the XPS signal (≈10 nm). Figure 2b,c shows the P 2p and Co 2p XPS scans at higher resolution over smaller energy windows, respectively. The binding energy of P 2p is at ≈133.28 eV, which is the characteristic peak of P in the phosphate group, confirming that P exists in the form of PO_4^{3-}. The characteristic peaks of Co $2p_{3/2}$ and Co $2p_{1/2}$ at around 781.58 and 797.38 eV are in the typical range of Co^{2+} and Co^{3+}, respectively.[47] The main Co $2p_{1/2}$ peak of the Co^{3+} ions generally appears between 794.0 and 794.7 eV, and the shift of this peak to a higher binding energy is indicative of an increase in the Co^{2+}/Co^{3+} ratio in the sample. However, the Co^{2+}/Co^{3+} ratio in the Co–Pi catalyst is not such important since the oxidation states of the Co ions are supposed to continuously change during the course of water oxidation reaction.[48]

The crystal structures and optical properties of the TiO_2, TiO_2/CdS, and TiO_2/CdS/Co–Pi nanowire arrays were further characterized by the X-ray diffractometer (XRD) and UV–vis absorption spectra. In **Figure 3**a, the XRD peaks collected from TiO_2 nanowire arrays on FTO substrate are indexed to the characteristic peaks of the tetragonal rutile TiO_2 (JCPDS 21-1276) and the substrate SnO_2 (JPCDS 77-0448). The absence of (110) peak of rutile TiO_2 at 2θ of 27.4 indicates the vertically standing morphology of the TiO_2 nanowires, in consistent with the SEM observation. The diffraction peaks for wurtzite CdS (JCPDS 41-1049) are indexed after the coating of CdS shell on the TiO_2. The XRD spectra of TiO_2/CdS/Co–Pi and TiO_2/CdS are indistinguishable. The absence of any nonFTO/TiO_2/CdS associated peaks in the triple composite photoanode indicates that the Co–Pi catalyst is amorphous. In the UV–vis absorption

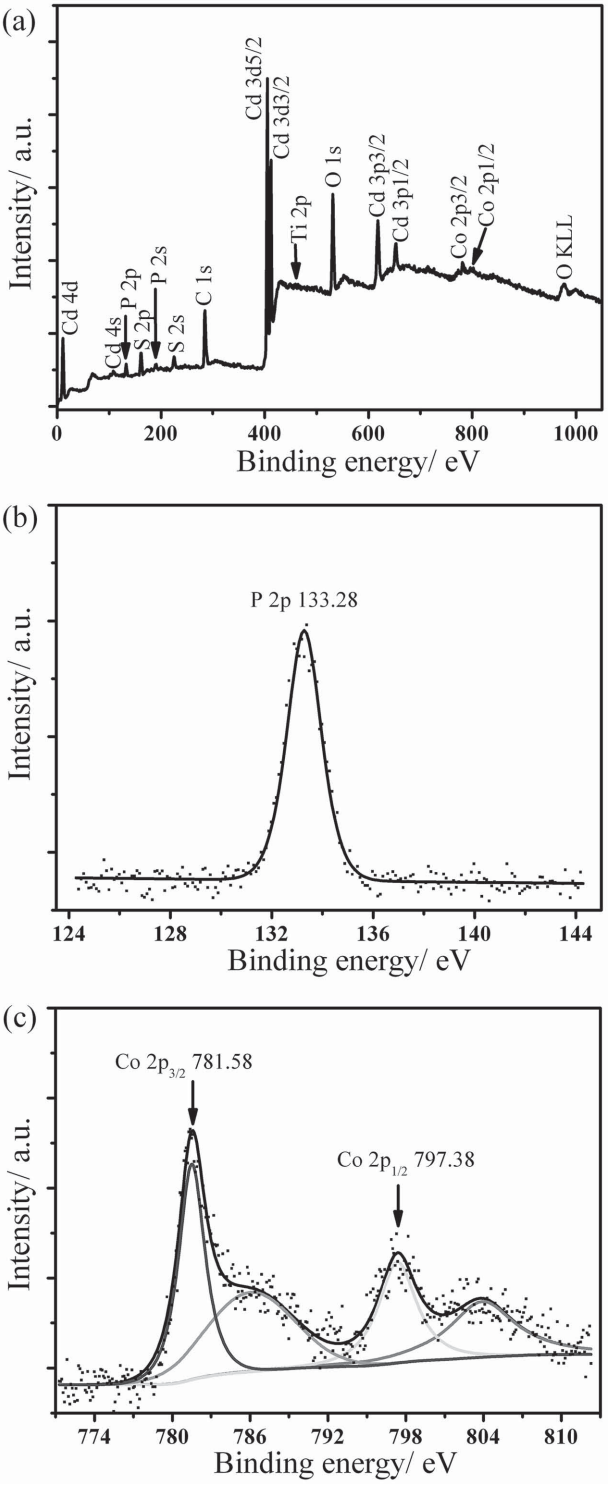

Figure 2. XPS survey scan from the TiO_2/CdS/Co–Pi composite electrode a) over a large range at low resolution, b) P 2p, and c) Co 2p at high resolution. The dark dots are the experimental results, and the dark curve is the summation of the gray synthetic peaks.

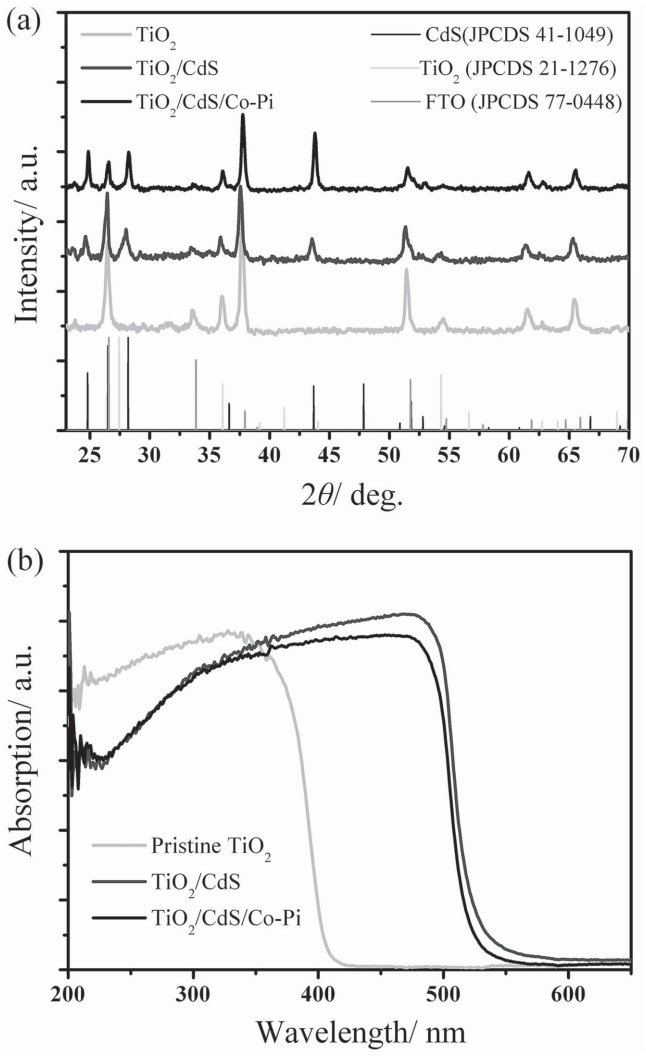

Figure 3. a) XRD patterns and b) UV–vis spectra of pristine TiO_2, TiO_2/CdS, and TiO_2/CdS/Co–Pi nanowire arrays on FTO substrates.

spectra (Figure 3b), the light absorption edge of TiO_2 is located at wavelength of ≈410 nm, in accordance with the 3.0 eV energy band gap (E_g) for rutile TiO_2. As light absorber, the CdS extends the light absorption of TiO_2/CdS electrode to visible region at the wavelength around 540 nm, corresponding to the E_g of 2.3 eV. The UV–vis spectra of TiO_2/CdS/Co–Pi show similar light absorption edge to TiO_2/CdS, implying no additional band gap transition induced by the Co–Pi catalyst. The UV–vis spectra of TiO_2/CdS/Co–Pi show similar light absorption features to TiO_2/CdS, implying no additional band gap transition induced by the Co–Pi catalyst. However, the Co–Pi catalyst probably may consume the incident light by nonproductive absorption,[31] thus all the PEC tests under light were carried out using a backside illumination method.

The PEC properties of these TiO_2-based nanowire array photoanodes were then investigated with a three-electrode PEC cell using a Pt foil as the counter electrode and Ag/AgCl as the reference electrode in 0.1 M sodium phosphate electrolyte (pH = 7). **Figure 4**a shows the photocurrent-voltage (*i*–*v*) curves of the bare TiO_2, TiO_2/CdS, and TiO_2/CdS/Co–Pi nanowire arrays in dark and under white-light illumination (AM 1.5G, 100 mW cm^{-2}). All samples show negligible background current under the dark conditions. It is noteworthy that the TiO_2/CdS/Co–Pi electrode needs much lower potential to drive obvious water oxidation reaction in dark, which can be ascribed to electrocatalyst effect of the Co–Pi, and also confirms the existence of Co–Pi on the TiO_2/CdS/Co–Pi sample. Upon irradiation, the TiO_2/CdS/Co–Pi nanowire array photoanode represents much higher photocurrent density than the TiO_2 or TiO_2/CdS nanowire arrays especially in the low external bias region. Moreover, the photocurrent onsets potential of TiO_2 nanowire arrays (i.e., –0.297 V vs Ag/AgCl) is gradually shifted to –0.403 V versus Ag/AgCl for TiO_2/CdS and then to –0.469 V versus Ag/AgCl for TiO_2/CdS/Co–Pi electrode. These shifts are due to the negatively shifted Fermi level[22] and decreased electron–hole recombination near the flat band potential[49] by CdS coating and the Co–Pi catalyzing, respectively. A more negative photocurrent onset potential is significantly important because it reduces the external bias needed for water oxidation reaction, and thus increases the overall efficiency of the PEC cells. Figure 4b represents the plots of the photoconversion efficiencies (i.e., solar energy to chemical fuel) as a function of the applied bias, which is deduced from Figure 4a using Equation (1)[50]

$$\eta = I(E^{\theta}_{\mathrm{rev}} - V)/J_{\mathrm{light}} \quad (1)$$

where I is the photocurrent density (mA cm^{-2}) at the measured bias, $E^{\theta}_{\mathrm{rev}}$ is the standard reversible potential for the water-splitting reaction, and V is the applied bias potential versus reversible hydrogen electrode (RHE). J_{light} is the irradiance intensity of 100 mW cm^{-2} (AM 1.5 G). Significantly, TiO_2/CdS/Co–Pi photoanode achieves the highest efficiency of 0.48% at a very low bias of 0.02 V versus Ag/AgCl, about 3.4 and 1.5 times higher than the TiO_2 (0.14% at bias of 0.1 V vs Ag/AgCl) and TiO_2/CdS (0.32% at bias of 0.09 V vs Ag/AgCl) photoelectrodes, respectively. Figure 4c shows the light photoresponse (*i*–*t*) curves of the TiO_2-based photoelectrodes measured at 0 V versus Ag/AgCl under chopped light irradiation. With the light "on" and "off" circles, the photocurrents of all photoelectrodes flashily rise up and drop down. These nearly vertical rising and falling photocurrents indicate that the charge transport in the photoelectrodes proceeds very quickly, which can be attributed to the direct electron transfer pathway provided by the 1D TiO_2 nanowire array nanomatrix. It is noteworthy that the "spikes" in photoresponse plots of the TiO_2/CdS/Co–Pi photoanode is much smaller than that of the TiO_2/CdS electrode, implying the much decreased electron–hole pair recombination in the TiO_2/CdS/Co–Pi photoanode after the Co–Pi modification. Figure 4d displays the *i*–*v* curves of the TiO_2, TiO_2/CdS, and TiO_2/CdS/Co–Pi photoelectrodes under visible light illumination (one sun illumination with a 420 nm long pass filter). As can be seen, while the pristine TiO_2 electrode exhibits a negligible photocurrent density of ≈7 μA cm^{-2}, the TiO_2/CdS and TiO_2/CdS/Co–Pi photoelectrodes both show more than 0.35 mA cm^{-2} saturated photocurrents under the visible light illumination, confirming the visible light response and light absorber role of the CdS in the composite photoelectrode.

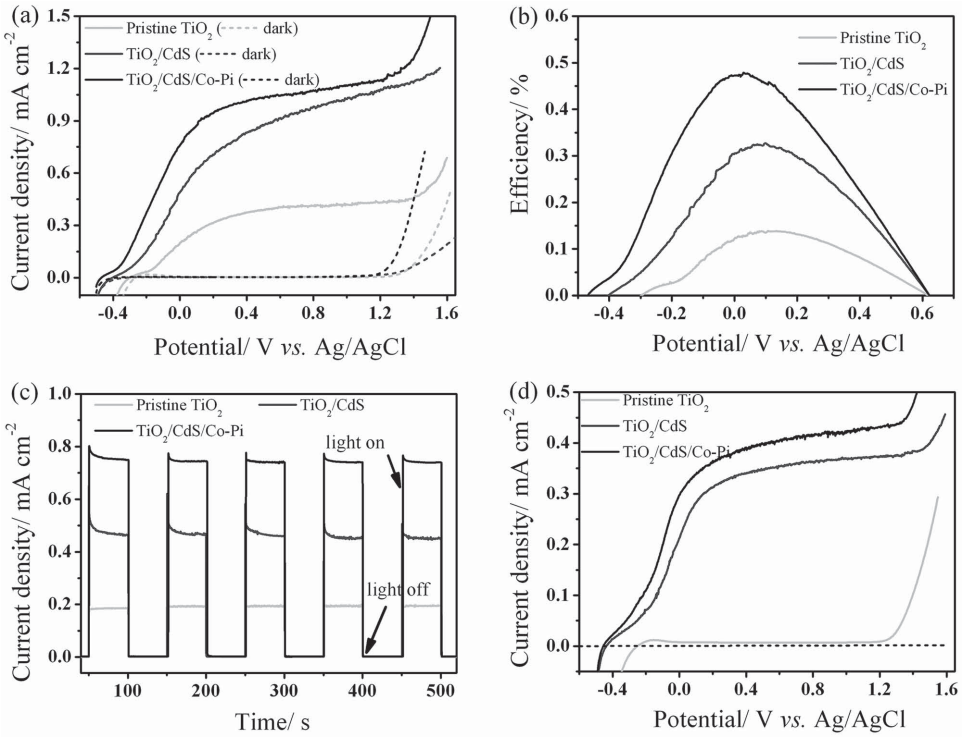

Figure 4. PEC measurements of the photoelectrodes in 0.1 M sodium phosphate electrolyte (pH = 7). a) *i–v* curves under white-light illumination, b) the calculated photoconversion efficiencies, and c) *i–t* curves measured at 0 V versus Ag/AgCl under chopped simulated sunlight illumination. d) *i–v* curves under visible-light illumination.

The PEC stability is a very important property for the solar hydrogen generation system particularly when the photocorrosion-susceptible chalcogenide compounds are involved. In this work, the stability of our photoanodes was investigated by 2 h water-splitting under simulated sunlight illumination in sodium phosphate solution (0.1 M, Ph = 7). During the measurement, a mall bias voltage of 0.6 V versus Ag/AgCl was applied between the photoanode and the Pt electrode to overcome additional ohmic losses in the electrolyte and metal contacts. In **Figure 5**a, the photocurrent of TiO_2/CdS electrode rapidly decays to a stable level of ≈0.4 mA cm^{-2} within 20 min. The rapid photocurrent decay is due to the poor anti-oxidation ability of the CdS in the photohole surroundings which induce the self-oxidative decomposition of CdS. As for the TiO_2/CdS/Co–Pi photoanode, its photocurrent also shows a relatively fast decline in the initial 25 min and then keeps at a relative stable level thereafter. However, the stable photocurrent of the TiO_2/CdS/Co–Pi photoanode is much higher than that of the TiO_2/CdS, with ≈0.69 mA cm^{-2} (72% of the initial photocurrent) retained after 2 h solar water splitting. The initial fast decrease of the photocurrent for the TiO_2/CdS/Co–Pi photoanode might be associated with the partial exposure of CdS to the electrolyte. The photograph of the electrodes are shown in the inset of Figure 5a, respectively marked as A, B, C, and D for the bare TiO_2, pristine TiO_2/CdS, and TiO_2/CdS/Co–Pi, TiO_2/CdS after stability test. The TiO_2/CdS/Co–Pi photoelectrode exhibits much slighter color fading than the TiO_2/CdS electrode after the stability measurement, suggesting that the photohole-induced self-oxidative decomposition of CdS is largely depressed by the Co–Pi WOC. The *i–v* curves of the electrodes were measured after the stability test and shown in Figure 5b. The TiO_2/CdS electrode shows similar *i–v* characteristic to the bare TiO_2 electrode, suggesting that the sensitization effect of the CdS on TiO_2 almost have vanished away and the photocurrent is mainly generated by the TiO_2 framework after the initial 20 min in Figure 5a. In contrast, the photocurrent of the TiO_2/CdS/Co–Pi electrode is still much higher than that of TiO_2 in the whole potential windows. As there still remains photocorrosion in the TiO_2/CdS/Co–Pi photoanode, efforts is being made to further increase its PEC stability by optimizing the Co–Pi modification.

The electrochemical impedance spectroscopy (EIS) measurements were carried out to explore the charge transfer and recombination processes at the electrode/electrolyte interfaces. The EIS Nyquist plots are collected at open-circuit conditions under simulated solar-light illumination and shown in **Figure 6**a. The experimental data dots are fitted into solid lines using the equivalent circuit model in the inset of Figure 6a. Here, R_s is the series resistance of the electrochemical device, CPE and R_{ct} are the capacitance phase element and the charge transfer resistance across the photoanode/electrolyte interface, respectively. The fitted values of R_{ct} are 3856, 2038, and 1367 Ω for TiO_2, TiO_2/CdS, and TiO_2/CdS/Co–Pi electrode, respectively. The smaller impedances of the composite electrodes than the pristine TiO_2 electrode can be ascribed to the formed type-II heterojunction interfaces and the enhanced charge carrier density under irradiation. The further decreased

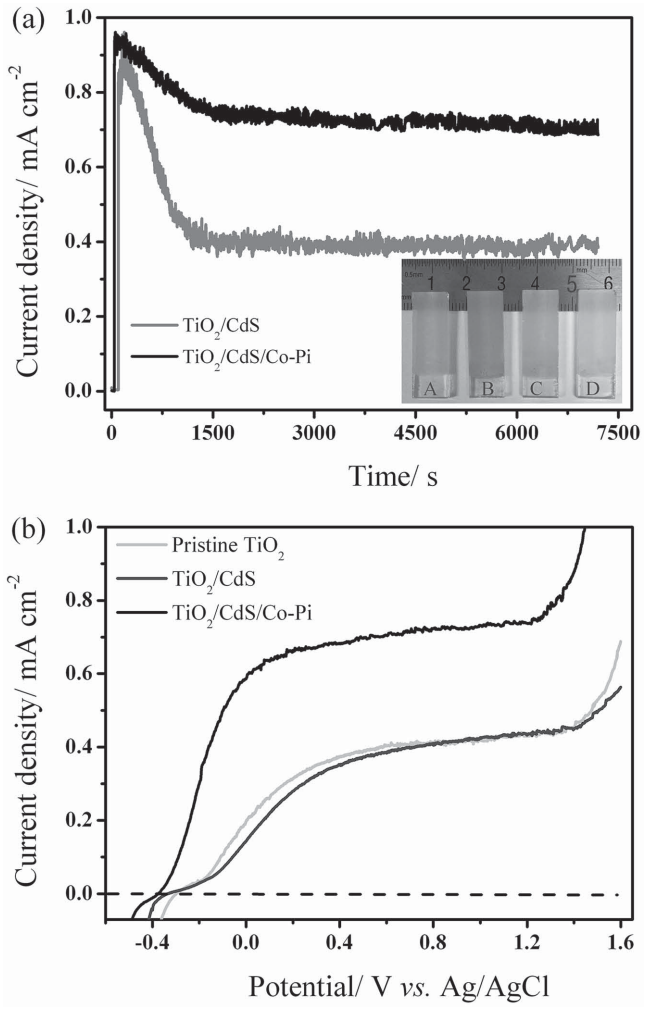

Figure 5. a) Steady-state photocurrents curves of TiO_2/CdS and TiO_2/CdS/Co–Pi photoelectrodes measured in 0.1 M sodium phosphate electrolyte (pH = 7) at 0.6 V versus Ag/AgCl under consistent one sun illumination for 2 h. The inset is the photograph of A: TiO_2, B: pristine TiO_2/CdS, C and D: TiO_2/CdS/Co–Pi and TiO_2/CdS after stability test, respectively. b) *i–ν* curves of TiO_2/CdS and TiO_2/CdS/Co–Pi photoelectrodes after 2 h stability test.

impedance of TiO_2/CdS/Co–Pi electrode indicates that the more favorable physicochemical environment for hole transfer from the electrode surface to electrolyte is created by the Co–Pi WOC. As a result, water oxidation was easier to realize due to the reduced charge transfer barrier as reported previously.[51] Thus, it is reasonably to reckon the introduced Co–Pi as a hole transfer accelerator at the electrode/electrolyte interfaces for fast surface chemical reactions.

To further understand the origin of the photoactivity enhancement for the ternary composite photoanode, the potential energy diagram for the TiO_2/CdS/Co–Pi composite film is determined. Assuming that the gap between the flat band potential (V_{FB}) and the conduction band bottom is negligible for n-type semiconductors, the conduction band position of TiO_2 and CdS can be estimated.[52] In Figure 6b, The V_{FB} at the electrode/electrolyte interfaces can be determined by extrapolating the X-intercepts of the linear region in the Mott–Schottky (M–S) curves, which are –0.36 and –0.25 V versus NHE (normal hydrogen electrode) for the TiO_2/CdS and TiO_2 electrode, respectively. The V_{FB} of TiO_2/CdS/Co–Pi is the same with the TiO_2/CdS electrode (–0.36 V vs NHE). The similar V_{FB} and M–S slope of TiO_2/CdS/Co–Pi with TiO_2/CdS electrode indicate that the Co–Pi nearly have no influence on the energy band level and charge carrier density of the electrode. In Figure 6c, the oxidation potential (E_{pa}) of the Co–Pi WOC is estimated by the cyclic voltammogram collected from the FTO/Co–Pi electrode, in which the Co–Pi WOC represents the anodic oxidation wave at 1.28 V versus NHE (E_{pa}) with a strong catalytic wave followed. Based on the above values (V_{FB} and E_{pa}) along with the E_g in Figure 3b, we constructed the potential energy diagram for the ternary composite electrode as shown in Figure 6d. The conduction band and valence band of CdS are more negative than the corresponding bands of TiO_2, demonstrating the type-II energy band alignment in the TiO_2/CdS/Co–Pi electrode. This thermodynamically favorable condition reduces the charge carrier recombination by the facile injection of the photogenerated electrons from the conduction band of CdS to that of the TiO_2. The reduced recombination would naturally induce photoactivity enhancement. In addition, the valence band potentials of TiO_2 and CdS, and the E_{pa} of Co–Pi WOC display a stepwise arrangement. As a WOC, the Co–Pi can catalyze the water oxidation reaction when the applied potential is larger than its E_{pa}. Thus, after combined with the TiO_2/CdS electrode, the Co–Pi WOC could use the valence band hole of the CdS to drive water oxidation reaction, accompanied by the fast output of photohole from TiO_2/CdS to water molecule (i.e., water oxidation). The facile charge transfer would reduce the hole accumulation on the electrode surfaces, which in return relieves the photogenerated electron–hole pair recombination (with enhanced photocurrent density) and hole-induced CdS self-oxidative decomposition (with improved PEC stability).

3. Conclusions

In summary, a novel material strategy has been proposed: the highly ordered 1D TiO_2/CdS/Co–Pi triple junction for PEC water splitting. This TiO_2/CdS/Co–Pi ternary composite photoanode exhibits much enhanced photocurrent especially in the low bias region, with 1.5 and 3.4 times improved photoconversion efficiency compared to the TiO_2/CdS and TiO_2 photoanode, respectively. More importantly, the PEC stability of the TiO_2/CdS nanowire array is significantly improved after the Co–Pi modification, with ≈72% of the initial photocurrent retained after 2 h persistent irradiation in stability test. Electrochemical impedance analysis indicates that the charge transfer between photoanode/electrolyte interface is largely accelerated by the Co–Pi mediator, which in return relieves the charge carrier recombination and photocorrosion of the CdS. This work provides a new paradigm for designing nanostructured backbone/light absorber/WOC ternary composite photoanode for efficient and stable solar fuel production, and is encouraging for application of this material designing strategy to other candidate photoanodes.

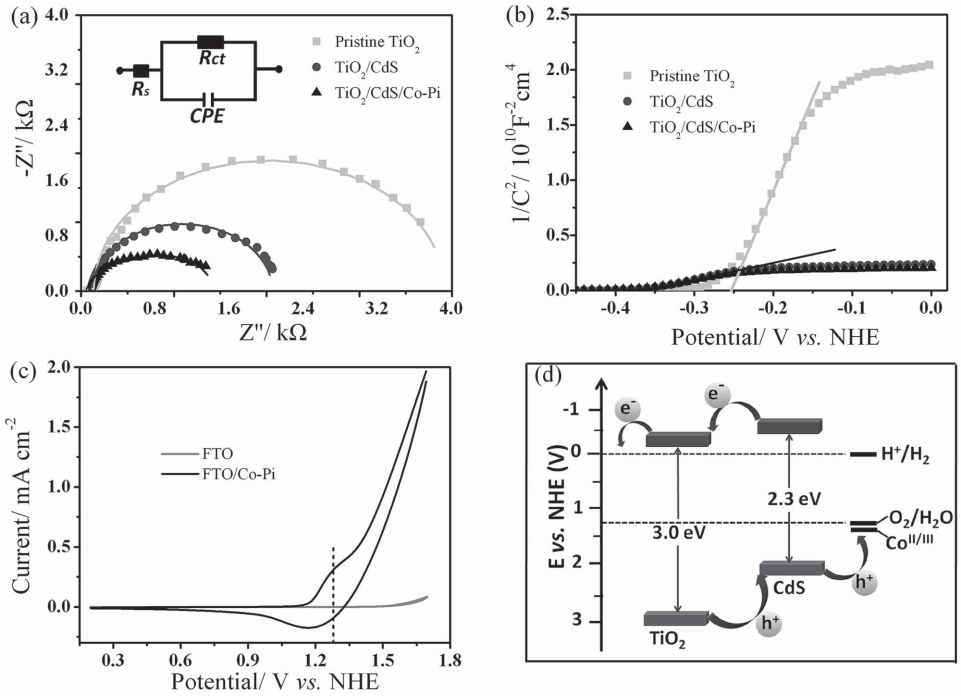

Figure 6. a) Nyquist plots and b) Mott–Schottky plots of the photoanodes. Inset in (a) is the equivalent circuit of the photoanode in the PEC cell. c) Cyclic voltammogram of FTO/Co–Pi electrode measured at a scan rate of 5 mV s^{-1}. d) Schematics of the potential energy diagram for the TiO_2/CdS/Co–Pi electrode.

4. Experimental Section

TiO_2/CdS/Co–Pi Triple Composite Nanowire Arrays Preparation: The TiO_2/CdS nanowire arrays were prepared according to our previous work in reference.[21] Briefly, hydrothermal method was used to grow TiO_2 nanowire arrays, followed by chemical vapor deposition process to coat the CdS shell or quantum dots (controlled by deposition time) on the TiO_2. The Co–Pi WOC (100 μC cm^{-2}) was deposited on the as-synthesized TiO_2/CdS nanowire array photoanode by photo-assisted electrodeposition in 0.1 M sodium phosphate buffer electrolyte containing 0.5 × 10^{-3} M cobalt nitrate under simulated one sun backside irradiation as described in our previous work in reference.[46]

Structural and Optical Characterizations: The morphology of the samples were characterized using the field emission SEM (NOVA NANOSEM 450, FEI, USA), and the microstructure was observed by transmission electron microscopy (JEM2010-HR, 200 KV) equipped with an EDS. The crystal structures were characterized by a Rigaku Dmax 2500 XRD with Cu K_α radiation. The surface composition and elemental chemical state of the samples were examined by XPS using a K-Alpha 1063 (Thermo Fisher Scientific, UK) equipped with Al Ka monochromator X-ray source. The light absorption was recorded by UV–vis spectrophotometer (UV-2500, Shimadzu, Japan).

PEC Measurements: The PEC measurements for the as-synthesized photoelectrodes were all carried out in 0.1 M sodium phosphate (ph = 7) electrolyte using a typical three-electrode configuration with a Pt foil as counter electrode and Ag/AgCl as reference electrode at an electrochemical workstation (CH Instruments, model CHI660E). The photocurrent–voltage (*i–v*) curves were measured at scan rate of 25 mV s^{-1} under simulated sunlight illumination using a 150 W Xe lamp as light source with the incident light intensity monitored to 100 mW cm^{-2} by a digital power meter. The light photoresponse (*i–t* curves) were evaluated under chopped light irradiation (light on/off cycles: 100 s) at a fixed electrode potential of 0 V versus Ag/AgCl. For visible light measurement, an additional 420 nm long pass filter was added to the light source. EIS Nyquist plots were collected under one sun illumination at open-circuit potential, with the frequency ranging from 100 kHz to 0.01 Hz and the modulation amplitude of 5 mV. To characterize the catalysis properties the Co–Pi WOC, Co–Pi was electrochemically deposited on FTO substrate at 1.1 V versus Ag/AgCl for 2 h in 0.1 M sodium phosphate electrolyte containing 0.5 × 10^{-3} M cobalt nitrate, which was further studied by cyclic voltammetry at scan rate of 5 mV s^{-1}. Mott–Schottky plots were measured in dark at an AC frequency of 1 kHz. For all PEC measurements, the active area of the working electrodes was strictly kept as 2 cm^2. The electrode potential versus Ag/AgCl is converted to the NHE potential according to the Nernst equations: $E_{NHE} = E_{Ag/AgCl} + E^{\theta}_{Ag/AgCl}$, where E_{NHE} are the converted potential versus NHE, $E^{\theta}_{Ag/AgCl}$ = 0.1976 V at 25 °C, and $E_{Ag/AgCl}$ is the experimental potential measured against the Ag/AgCl reference electrode.

Acknowledgements

The authors thank the financial support of the National Natural Science Foundation of China (Grant nos. 51202208, 51172191, and 11274264), National Basic Research Program of China (Grant no. 2012CB921303), and the Program for Changjiang Scholars and Innovative Research Team in University (IRT13093).

Received: June 16, 2015
Revised: July 19, 2015
Published online: August 11, 2015

[1] J. Barber, *Chem. Soc. Rev.* **2009**, *28*, 185.
[2] A. Fujishima, K. Honda, *Nature* **1972**, *238*, 37.
[3] P. V. Kamat, K. Tvrdy, D. R. Baker, J. G. Radich, *Chem. Rev.* **2010**, *110*, 6664.

[4] H. M. Chen, C. K. Chen, R. Liu, L. Zhang, J. Zhang, D. P. Wilkinson, *Chem. Soc. Rev.* **2012**, *41*, 5654.
[5] S. J. A. Moniz, J. Zhu, J. Tang, *Adv. Energy Mater.* **2014**, *4*, 1301590.
[6] J. Sun, D. K. Zhong, D. R. Gamelin, *Energy Environ. Sci.* **2010**, *3*, 1252.
[7] Y. Wang, Q. Wang, X. Zhan, F. Wang, M. Safdar, J. He, *Nanoscale* **2013**, *5*, 8326.
[8] C. Cheng, H. Zhang, W. Ren, W. Dong, Y. Sun, *Nano Energy* **2013**, *2*, 779.
[9] C. Wang, Z. Jiang, L. Wei, Y. Chen, J. Jiao, M. Eastman, H. Liu, *Nano Energy* **2012**, *1*, 440.
[10] Y. Wang, Q. Wang, X. Zhan, F. Wang, M. Safdar, J. He, *Nanoscale* **2013**, *5*, 8326.
[11] Y. Liu, L. Zhao, M. Li, L. Guo, *Nanoscale* **2014**, *6*, 7397.
[12] J. Lee, T. G. Kim, H. Choi, Y. Sung, *Cryst. Growth Des.* **2007**, *7*, 2588.
[13] J. H. Bang, P. V. Kamat, *Adv. Funct. Mater.* **2010**, *20*, 1970.
[14] C. Yao, B. Wei, L. Meng, H. Li, Q. Gong, H. Sun, H. Ma, X. Hu, *J. Power Sources* **2012**, *207*, 222.
[15] S. A. Vanalakar, S. S. Mali, R. C. Pawar, N. L. Tarwal, A. V. Moholkar, J. H. Kim, P. S. Patil, *J. Appl. Phys.* **2012**, *112*, 44302.
[16] K. S. Leschkies, R. Divakar, J. Basu, E. Enache-Pommer, J. E. Boercker, C. B. Carter, U. R. Kortshagen, D. J. Norris, E. S. Aydil, *Nano Lett.* **2007**, *7*, 1793.
[17] C. Eley, T. Li, F. Liao, S. M. Fairclough, J. M. Smith, G. Smith, S. C. E. Tsang, *Angew. Chem. Int. Ed.* **2014**, *53*, 7838.
[18] Y. Zhang, Z. Wu, J. Zheng, X. Lin, H. Zhan, S. Li, J. Kang, J. Bleuse, H. Mariette, *Sol. Energy Mater. Sol. Cells* **2012**, *102*, 15.
[19] W. Chen, N. Zhang, N. Y. Zhang, X. T. Zhang, H. Gao, J. Wen, *Cryst. Eng. Commun.* **2014**, *16*, 1201.
[20] G. Ai, R. Mo, H. Xu, Q. Chen, S. Yang, H. Li, J. Zhong, *J. Power Sources* **2015**, *280*, 5.
[21] G. Ai, R. Mo, H. Xu, Q. Chen, S. Yang, H. Li, J. Zhong, *J. Appl. Phys.* **2014**, *116*, 174306.
[22] J. Luo, L. Ma, T. He, C. F. Ng, S. Wang, H. Sun, H. J. Fan, *J. Phys. Chem. C* **2012**, *116*, 11956.
[23] T. K. Sung, J. H. Kang, D. M. Jang, Y. Myung, G. B. Jung, H. S. Kim, C. S. Jung, Y. J. Cho, J. Park, C. Lee, *J. Mater. Chem.* **2011**, *21*, 4553.
[24] Z. Chen, W. Peng, K. Zhang, J. Zhang, M. Yanagida, L. Han, *Nanoscale* **2012**, *4*, 7690.
[25] K. Cheng, X. Han, J. Meng, S. Wang, Z. Du, *RSC Adv.* **2015**, *5*, 11084.
[26] H. Li, C. Cheng, X. Li, J. Liu, C. Guan, Y. Y. Tay, H. J. Fan, *J. Phys. Chem. C* **2012**, *116*, 3802.
[27] Q. Luo, Z. Wu, J. He, Y. Cao, W. A. Bhutto, W. Wang, X. Zheng, S. Li, S. Lin, L. Kong, J. Kang, *Nanoscale Res. Lett.* **2015**, *10*, 181.
[28] X. Zhan, Q. Wang, F. Wang, Y. Wang, Z. Wang, J. Cao, M. Safdar, J. He, *ACS Appl. Mater. Interfaces* **2014**, *6*, 2878.
[29] X. Chen, S. Shen, L. Guo, S. S. Mao, *Chem. Rev.* **2010**, *110*, 6503.
[30] J. Li, N. Wu, *Catal. Sci. Technol.* **2015**, *5*, 1360.
[31] M. de Respinis, K. S. Joya, H. J. M. De Groot, F. DSouza, W. A. Smith, R. van de Krol, B. Dam, *J. Phys. Chem. C* **2015**, *119*, 7275.
[32] L. Wang, F. Dionigi, N. T. Nguyen, R. Kirchgeorg, M. Gliech, S. Grigorescu, P. Strasser, P. Schmuki, *Chem. Mater.* **2015**, *27*, 2360.
[33] J. H. Kim, J. W. Jang, H. J. Kang, G. Magesh, J. Y. Kim, J. H. Kim, J. Lee, J. S. Lee, *J. Catal.* **2014**, *317*, 126.
[34] Y. Zhang, C. Zhao, X. Dai, H. Lin, B. Cui, J. Li, *J. Power Sources* **2013**, *243*, 908.
[35] M. Seol, J. Jang, S. Cho, J. S. Lee, K. Yong, *Chem. Mater.* **2013**, *25*, 184.
[36] M. Zhong, T. Hisatomi, Y. Kuang, J. Zhao, M. Liu, A. Iwase, Q. Jia, H. Nishiyama, T. Minegishi, M. Nakabayashi, N. Shibata, R. Niishiro, C. Katayama, H. Shibano, M. Katayama, A. Kudo, T. Yamada, K. Domen, *J. Am. Chem. Soc.* **2015**, *137*, 5053.
[37] M. Liao, J. Feng, W. Luo, Z. Wang, J. Zhang, Z. Li, T. Yu, Z. Zou, *Adv. Funct. Mater.* **2012**, *22*, 3066.
[38] D. A. Lutterman, Y. Surendranath, D. G. Nocera, *J. Am. Chem. Soc.* **2009**, *131*, 3838.
[39] C. C. L. McCrory, S. Jung, I. M. Ferrer, S. M. Chatman, J. C. Peters, T. F. Jaramillo, *J. Am. Chem. Soc.* **2015**, *137*, 4347.
[40] G. M. Carroll, D. K. Zhong, D. R. Gamelin, *Energy Environ. Sci.* **2015**, *8*, 577.
[41] Y. Surendranath, M. W. Kanan, D. G. Nocera, *J. Am. Chem. Soc.* **2010**, *132*, 16501.
[42] S. K. Pilli, T. E. Furtak, L. D. Brown, T. G. Deutsch, J. A. Turner, A. M. Herring, *Energy Environ. Sci.* **2011**, *4*, 5028.
[43] G. M. Carroll, D. K. Zhong, D. R. Gamelin, *Energy Environ. Sci.* **2015**, *8*, 577.
[44] J. A. Seabold, K. Choi, *Chem. Mater.* **2011**, *23*, 1105.
[45] Y. Li, T. Takata, D. Cha, K. Takanabe, T. Minegishi, J. Kubota, K. Domen, *Adv. Mater.* **2013**, *25*, 125.
[46] G. Ai, R. Mo, H. Li, J. Zhong, *Nanoscale* **2015**, *7*, 6722.
[47] M. Shao, F. Ning, M. Wei, D. G. Evans, X. Duan, *Adv. Funct. Mater.* **2014**, *24*, 580.
[48] D. K. Zhong, D. R. Gamelin, *J. Am. Chem. Soc.* **2010**, *132*, 4202.
[49] E. M. P. Steinmiller, K. Choi, *Proc. Natl. Acad. Sci. USA* **2009**, *106*, 20633.
[50] Y. Mao, H. Yang, J. Chen, J. Chen, Y. Tong, X. Wang, *Nano Energy* **2014**, *6*, 10.
[51] Q. Yu, X. Meng, T. Wang, P. Li, J. Ye, *Adv. Funct. Mater.* **2015**, *25*, 2686.
[52] S. J. Hong, S. Lee, J. J. Suk, L. J. Sung, *Energy Environ. Sci.* **2011**, *4*, 1781.